AN APPROACH TO THE GUST PROBLEM WITH INTERFERING PROFILES

W. Send

German Aerospace Center (DLR), Institute of Aeroelasticity
Bunsenstr. 10, D-37073 Göttingen, Germany
e-mail: wolfgang.send@dlr.de

Keywords: Gust Load, Interference, Unsteady Aerodynamics, Viscous Flow, Vorticity.

Abstract. The mutual influence of two profiles is studied in subsonic and transonic 2D viscous flow. The profiles are arranged such that the second one is located downstream of the first one similar to the configuration of a tail plane behind a wing. The physical effect is that of a gust generator. The unsteady wake of the leading profile encounters the trailing profile and effects a load change. A first simplified attempt has been made using a rigid grid where both profiles execute a synchronous heaving motion. Similar results of a 3D computation show the generation of the unsteady wake interacting with the boundary layer along a viscous wall which represents one side of a wind tunnel.

1 INTRODUCTION

The physical phenomena occurring during a gust event have been investigated in the past primarily on an experimental basis. The very first experiment dates back to Katzmayr in 1922, who uses the new wind tunnel at the Aeromechanical Laboratory of the Royal Technical University in Vienna [1]. His work serves as an example for subsequent research using a gust generator [2]. An overview of research in the second half of the last century may be found in [3]. More recent work concentrates on the wake itself behind large transport aircraft [4].

Modern CFD provides access to a detailed analysis of the interaction between a gust field and an aircraft wing it acts on. The work presented here is a first step towards a broader numerical approach to a 3D configuration with more flexible kinematics. The numerical framework is the DLR Tau code [5]. An earlier version of the contents was presented at a German conference [6].

The study prepares for several wind tunnel experiments in the DLR's 1x1 square meter transonic wind tunnel within the DLR project iGREEN. The physical effect is that of a gust generator: The unsteady wake of the leading profile encounters the trailing profile and effects a load change. Figure 1 shows a typical subsonic solution. A first simplified attempt has been made using a rigid grid where both profiles execute a synchronous heaving motion. This simplification avoids additional numerical implications caused by the chimera grid generation technique, which needs to be applied for profiles being in motion relative to each other. After the motion is turned off, the vorticity shed from the leading profile carries a single gust event downstream to the second profile. The Fourier analysis of the load history shows the load spectrum. Besides the main purpose of the computations to predict gust loads, the unsteady flow field with the physical data given below shows interesting features like the interaction of two wakes, the generation and propagation of sound waves and the impact of incoming vorticity on a shock front, where almost all of the supersonic domain literally is blown out.

The study also includes basic research on the accuracy of the numerical calculations, which rest on the DLR Tau code. The conservation of advected vorticity is investigated behind the

leading profile as well as the propagation of sound waves travelling upstream of the trailing profile. The total circulation during one cycle of motion behind an oscillating wing is supposed to be zero at any downstream position, which is an intrinsic check for the whole proper setting of physical und numerical parameters. In the given examples, the ratio of total circulation over one period to the respective amplitude of the vorticity, i.e. the numerical error, is less than 1 %.

The 3D results show the formation of the unsteady wake vortices along the viscous wall which consist of distorted rings. The distortion is a consequence of the deceleration of the flow along the wall. In the few computations completed so far, the delay is up to half a period. The very first computations presented here rest on a fairly coarse grid which increases the numerical error up to about 10 %.

2 SOLUTION PARAMETERS AND STEADY SOLUTION

The numerical characteristics of the solution scheme employed are

- central differences for the discretization of the fluxes for the Reynolds averaged Navier-Stokes equations (RANS) with the Spalart-Allmaras turbulence model applying Edwards' modification (SAE),
- dual time-stepping with 200 inner iterations during two subsequent physical time steps, which divide one period of motion into 360 steps,
- multi-grid procedure with 5 levels of resolution, using backward Euler relaxation for the implicit time integration and a symmetric Gauß-Seidel decomposition ((LUSGS).

The unstructured grid has been generated using CENTAUR software. The total number of points is 289,406. 325,762 triangles and 124,440 quadrilaterals for the boundary layer form the mesh. With 30 prismatic layers, each profile boundary is formed by 2,074 quadrilateral baselines. The computational grid is displayed in Figure 2. The distance h of the first layer to the wall is $h(1) = 1.2\ 10^{-5}$. The chord length c is 1 m. The kinematics are

- a synchronous heaving motion with an amplitude $h_0/c = 0.1$,

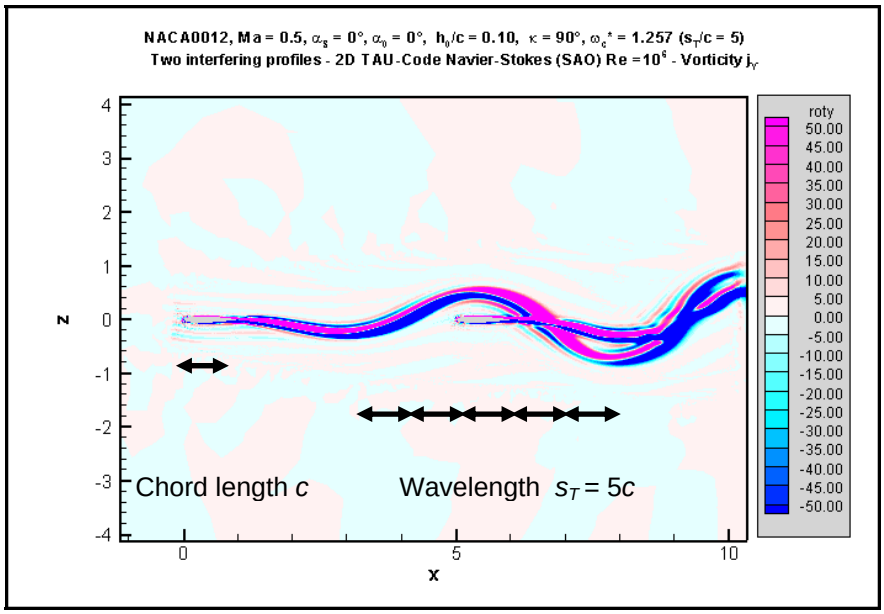

Figure 1: Configuration of the two oscillating profiles with a typical wake.

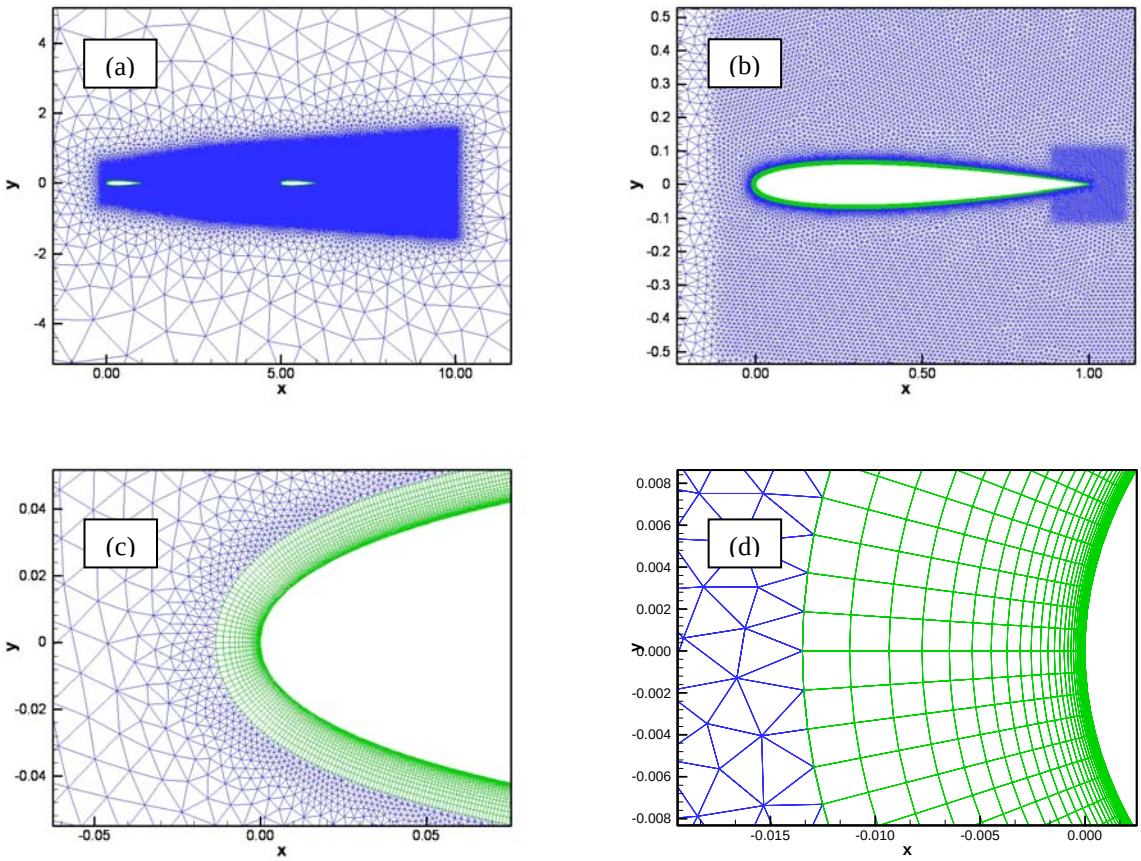

Figure 2: The 2D mesh for the two profiles NACA0012. (a) displays the whole computational domain, (b) the leading profile with a finer resolution around the trailing edge, (c) the leading edge with transition to triangles, and (d) a close view on the leading edge.

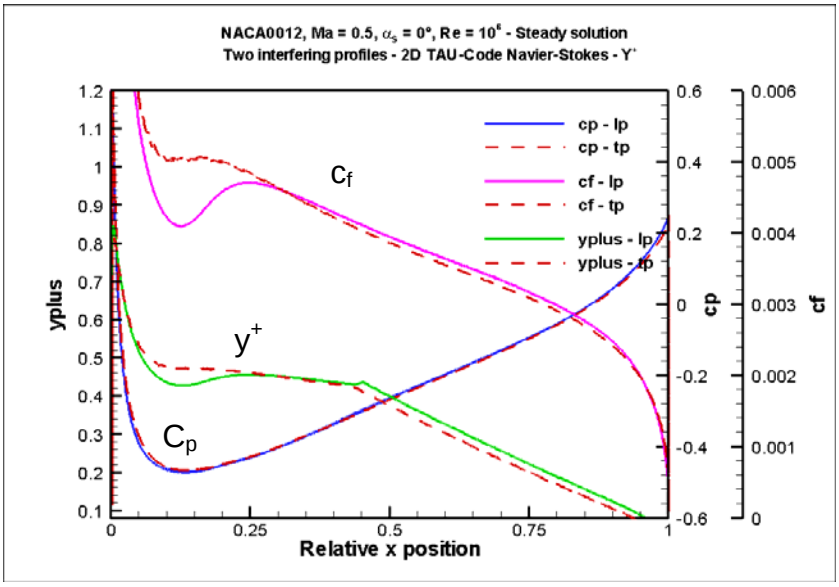

Figure 3: Steady subsonic solution, Ma = 0.5, Re = 10^6, angle of incidence α_S = 0 deg for both the leading profile (lp) and the trailing profile (tp).

- two pairs of Mach number and Reynolds number (*Ma*, *Re*) = (0.5, 10^6) and (0.75,10^7) for subsonic and transonic flow with velocities 165.8 m/s and 248.6 m/s, based on the speed of sound c_S = 331.5 m/s,

- the reduced frequency $\omega^* = 2\pi/5 = 1.257$ (based on c), leading to a natural frequency f of 33.3 Hz for $Ma = 0.5$ and of 50 Hz for $Ma = 0.75$.

The spatial distance between the trailing edge (TE) of the first profile and the leading edge (LE) of the second profile is 4 c (c = 1 m). The fairly high reduced frequency is chosen such that the wake length for one period of motion fits into the area of fine grid resolution covering the space around the two profiles.

The properties of the steady subsonic solution shows Figure 3. There is hardly any influence of the profiles on each other in steady flow. The two coefficients for pressure c_p and friction c_f look very similar. The characteristic numerical value y^+ is in the order of 1 as desired.

3 ESTIMATE OF ACCURACY: VORTICITY AND SOURCE DENSITY

A matter of concern is the estimate of accuracy. For computational fluid dynamics, there is no mathematically satisfying way at hand to proof the accuracy of a solution. The frequently used residual margins, e.g. the density residual, are without physical meaning. They may indicate a convergence of the solution in the order of 10^{-5} to 10^{-10}. Nevertheless the physically meaningful accuracy will be much worse. The following two figures illustrate the statement:

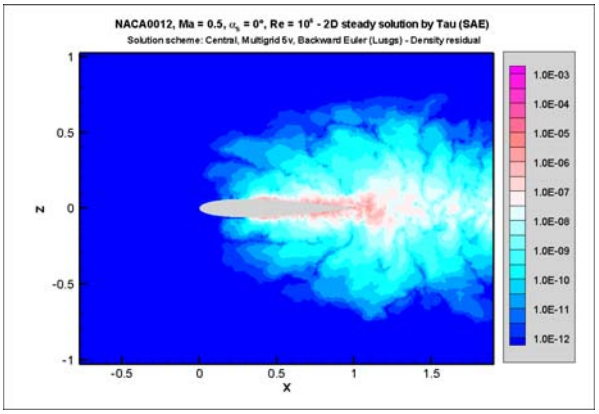

Figure 4: Density residual of the subsonic solution.

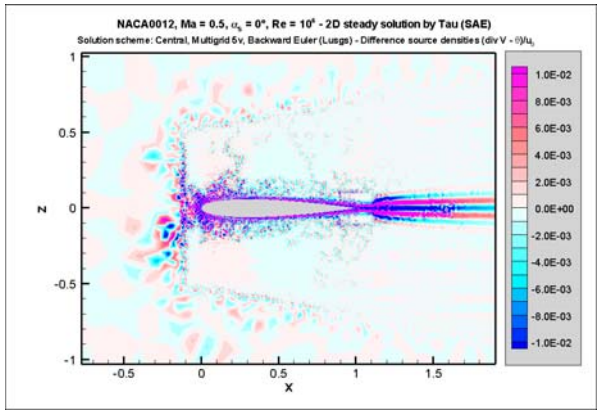

Figure 5: Absolute error via source density.

Figure 4 shows the contour plot of the density residual in the vicinity of the leading profile. The figure clearly indicates that the solution better converges in regions with increasing distance to the profile. There is no relation visible to the decreasing quality of the grid more distant to the profile as plotted in Figure 2 (a). Opposite to the density residual, the contour plot in Figure 5 shows a particularly granular structure of larger absolute values along the border which separates the fine grid from the coarse far field grid in Figure 2 (a). The other grainy area is found around the profile. The function plotted is the difference between two other functions. Both functions represent the divergence *div* **v** of the flow field. The two functions stem from one and the same numerical solution. The way the differ from each other reflects the numerical accuracy of the computed solution. This relationship now is discussed in more detail.

3.1 The Conservation Laws, Vorticity and Source Density

Essentially, the solution of flow problems aims at determining the reaction force of the fluid on a body moving in it. Two basically different approaches exist for solving the conservation laws for momentum, mass and energy. The integral representation of the conservation laws

uses the density functions source density $\delta = div\ \mathbf{v}$ and vorticity $\mathbf{j} = curl\ \mathbf{v}$. Following the fundamental theorem in vector analysis, each vector field may be represented by the potentials of these two density functions. Source density is related to the fluid's property being compressible, vorticity (vortex density) reflects the fluid's property being viscous. The solution algorithms are governed by the global discretization of the field functions and their instant or retarded distant influence on the solution. The differential representation of the conservation laws uses the flux vector densities mass flux density $\rho\,\mathbf{v}$, momentum flux density $p\mathbf{n}+\rho\,\mathbf{v}(\mathbf{v}\cdot\mathbf{n})$ and energy flux density $\rho\,\mathbf{v}(\mathbf{v}^2/2+e+p/\rho)$.

All three fluxes always remain conserved, and thus are applicable for a local discretization. The material properties exist besides a fixed number of variables. The solution algorithms are governed by the local discretization of the flux vector functions. Their local influence transfers the solution to neighboring flow domains.

The physically motivated estimate of accuracy follows the concept to use the integral representation for a numerical check how well a solution preserves the properties of source density and vorticity.

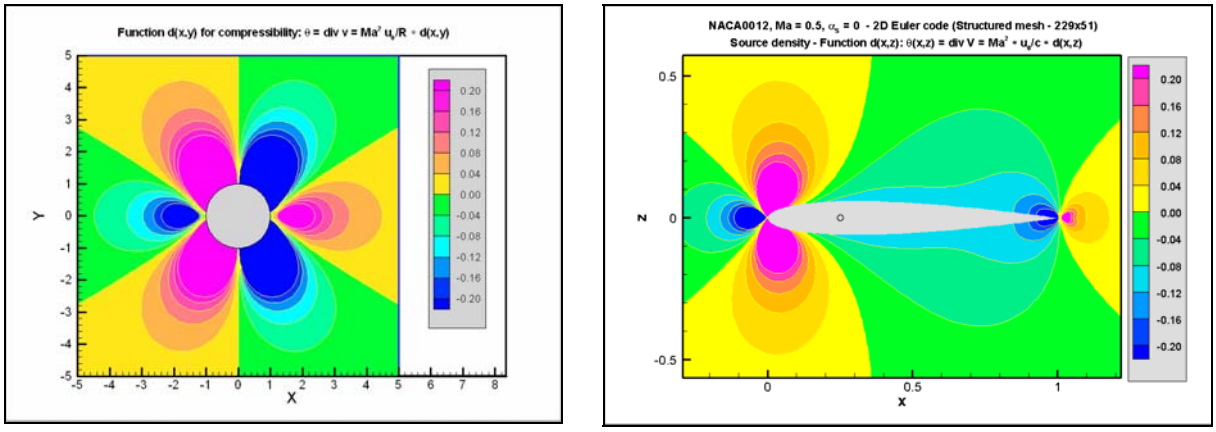

Figure 6: Source densities of the 2D circular cylinder (analytical solution based on functional theory) and of the NACA0012 profile (numerical solution based on a structured Euler code).

3.2 Source Density in Subsonic Flow

Different from the conservation of momentum and energy, the conservation law for mass is a purely kinematical property of a fluid with density ρ and its inverse $\upsilon = 1/\rho$, which describes the isotropic expansion:

$$\dot{\upsilon} = \delta \cdot \upsilon, \quad \delta = div\mathbf{v}, \quad \upsilon = 1/\varrho, \quad or \quad \dot{\varrho} + \varrho \cdot div\mathbf{v} = 0 \tag{1}$$

The time derivative of ρ refers to material coordinates and reads for constant entropy s:

$$\frac{d\varrho}{dt} = \left(\frac{d\varrho}{dp}\right)_S \cdot \frac{dp}{dt}, \quad with \quad \left(\frac{d\varrho}{dp}\right)_S = c_s^2(p) \quad \Rightarrow \quad \delta \equiv div\mathbf{v} = -\frac{1}{\varrho \cdot c_s^2} \cdot \frac{dp}{dt} \tag{2}$$

c_S is the velocity of sound. Equation (2) relates the source density to the time derivative of the pressure. Next the pressure is replaced by the definition of the pressure coefficient c_P. So far the relation holds true without restrictions. In steady incompressible flow without viscosity, the pressure coefficient reduces to Bernoulli's Equation:

$$c_P\left(\mathbf{x}\right) := \frac{p(\mathbf{x})-p_\infty}{\frac{1}{2}\ \varrho_\infty \cdot u_0^2} = 1 - \left[\frac{\mathbf{v}(\mathbf{x})}{u_0}\right]^2 \tag{3}$$

The right part in Equation (3) reduces to the following relation for the present case of a 2D solution with coordinates *(x,z)* and velocity components *(u,w)*:

$$div\ \mathbf{v}\ \ =\ \ \theta = -\tfrac{1}{2}Ma^2\ \left[u(x,z)\cdot\frac{\partial c_p(x,z)}{\partial x} + w(x,z)\cdot\frac{\partial c_p(x,z)}{\partial z}\right] \tag{4}$$

The partial derivates of c_P are found by applying Equation (3). Figure (5) shows the contour plot of the function

$$(\delta(x,z) - \theta(x,z))/u_0 \tag{5}$$

u_0 is the free-stream velocity. The difference between the two definitions of the source density named δ and θ is supposed to be zero only in regions without viscosity and, of course, for incompressible flow. Thus, the increasing absolute value close to the surface and in the wake is due to the boundary layer and the viscous wake domain. The low Mach number plays a minor role.

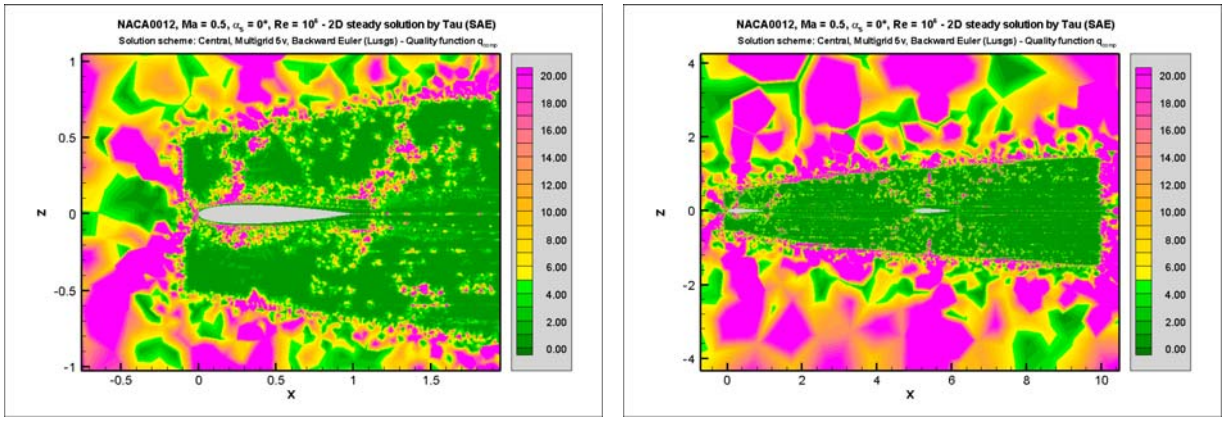

Figure 7: Quality function measured using the subsonic solution.

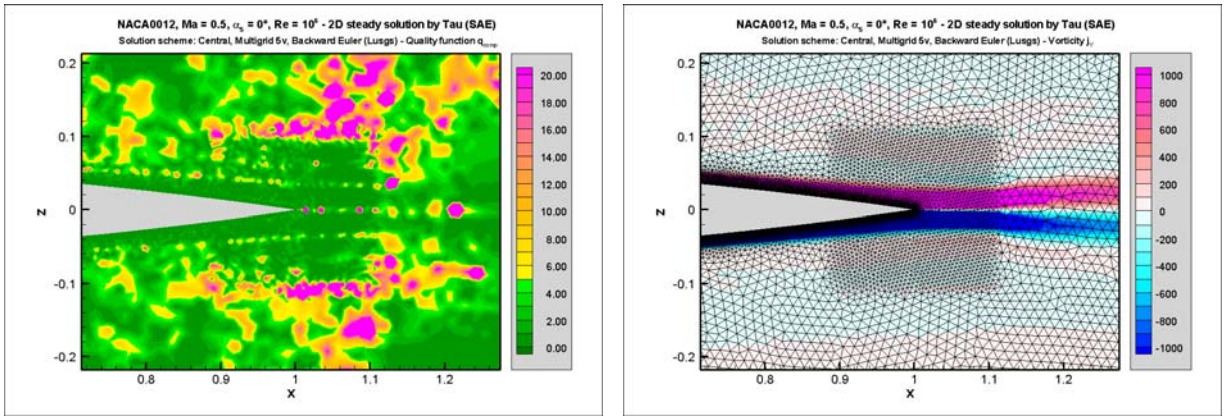

Figure 8: Quality function for areas with different grid resolutions.

Equation (4) is of general importance for understanding the conceptual limitations of what is frequently called an *exact solution* for the flow in an "ideal incompressible fluid", based on the assumption of *div* **v** = 0. None of these solutions is exact with respect to the conservation

laws, and Equation (4) shows the error. The contour plots of the source density in Aerodynamics display an unique topology of alternating zones with compression and expansion. Figure (6) shows two typical plots, which are normalized by the square of Mach number times free-stream velocity divided by chord length.

The comparison of the two source density functions is made for subsonic flow. It takes aim at a relation between the designed grid and the numerical code. It is supposed to reveal inadequate settings for the grid generation as well as to indicate the quality of the numerical treatment. As already mentioned, the validity of Equation (5) is limited to regions without vorticity. The data in Figure 5 are differences which do not weigh the magnitude of the values. The relative computational error is obtained by dividing the difference δ - θ by the function *max*(*abs*(δ),10^{-10}). The limitation is necessary to avoid division by zero along the lines where the source density changes its sign (Figure 6). The misleading high values of δ - θ in the boundary layer and the wake can be eliminated by a modified definition for these regions. The *max* function is extended by the magnitude *abs*(j_y) of the vorticity and now reads *max*(*abs*(δ),*abs*(j_y),10^{-10}). These manipulations lead to a function which may be called the quality function q_{comp} of the numerical computation:

$$q_{comp}(x,z) := \frac{abs(\delta(x,z)-\theta(x,z))}{max(abs(\delta(x,z)),abs(j_y(x,z)),10^{-10})} \cdot 100 \ \ [\%] \tag{6}$$

The result of the quality function applied to the grid in Figure 2 together with the DLR Tau code is displayed in Figure 7. The colour map changes from green to yellow at 5 %, which is an arbitrarily chosen value. The overall impression is that the solution in the region of the fine grid leads to a fairly reasonable accuracy in the order of 5 %. However, the small box with a finer grid at the trailing edge in Figure 8 shows almost no yellow spots. The figures make a further diagnosis: The change from the fine resolution area to the less fine resolution area takes place too rapidly and thereby causes local disturbances in the solution. A redesign of the grid is advisable.

Nevertheless, the expectation is justified that a gust generated by the leading profile is transported to the trailing profile without significant losses in strength.

3.3 Vorticity and Conservation of Circulation

First the *curl* operator is applied to the momentum equation and the assumption is made that terms with products of viscosity and compressibility are small and can be neglected. This step is some kind of a *physical linearization.* The result is the vorticity transport equation in subsonic flow [7]. This equation shows that the scalar flux of the vorticity field through a commoving surface is preserved if no diffusion of vorticity into the neighborhood of the surface takes place. The vorticity transport equation reads:

$$\frac{d}{dt}\mathbf{j}(\mathbf{x},t) = \mathbf{j}(\mathbf{x},t) \cdot grad\mathbf{v}(\mathbf{x},t) + \frac{\eta}{\varrho(p)}\Delta\mathbf{j}(\mathbf{x},t) - \theta \cdot \mathbf{j}(\mathbf{x},t) \tag{7}$$

Helmholtz' transport theorem for the scalar flux $\delta\Phi$ of an arbitrary vector field **f** through a commoving surface element δS states:

$$\frac{d}{dt}\delta\Phi = \left[\frac{d}{dt}\mathbf{f} - \mathbf{f} \cdot grad\mathbf{v} + div\mathbf{v} \cdot \mathbf{f}\right] \cdot \delta S \tag{8}$$

v is the vector field of the fluid. Equation (7) is rearranged using the transport theorem

$$\frac{d}{dt}\delta\Gamma = \left[\frac{d}{dt}\mathbf{j} - \mathbf{j}\cdot grad\mathbf{v} + \theta\cdot\mathbf{j}\right]\cdot\delta S = \left[\frac{\eta}{\varrho(p)}\Delta\mathbf{j}\right]\cdot\delta S \tag{9}$$

with the definition of the scalar flux of **j**, the circulation,

$$\Gamma(\mathbf{j},t) = \int\int_S \mathbf{j}(\mathbf{y},t)\cdot d\mathbf{S}(\mathbf{y}) = \int\int_S \delta\Gamma(\mathbf{j},t) \tag{10}$$

If a surface *S* is placed perpendicular to the flow and laid out sufficiently large, then all of the vorticity shed downstream from a lifting wing is captured. For such a surface, the circulation Γ has to vanish at any time for a steady solution and over a period *T* of motion for an unsteady solution.

$$Steady\ \ case: \ \ \Gamma(\mathbf{j}) = \ \ 0, \ \ Unsteady\ \ case: \int_0^T \Gamma(\mathbf{j},t)\cdot dt = \ \ 0 \tag{11}$$

Figure 9 shows the location of the integration paths for the steady and the unsteady cases.

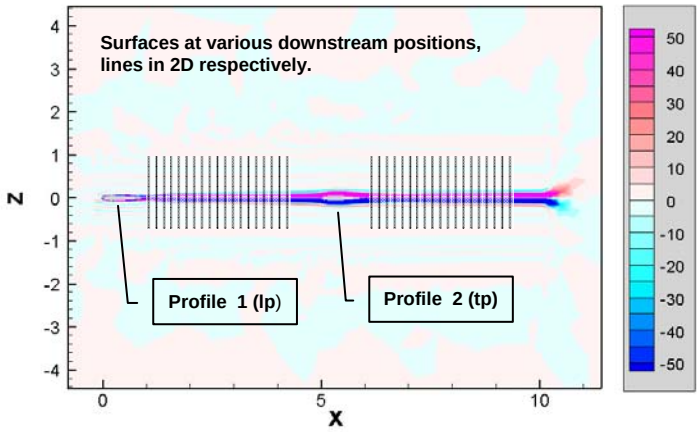

Figure 9**:** Location of the 2 profiles, contours of the vorticity field of the steady solution, j_Y ranging from -50 to 50 1/s for Ma = 0.5, integration paths.

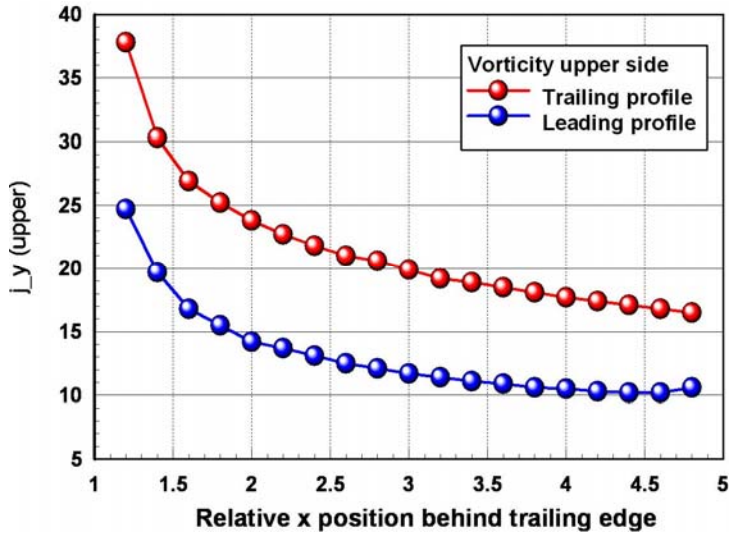

Figure 10**:** Integration of vorticity in the upper half (z > 0) of the respective wake.

The vorticity field **j** (*x*,*y*,*z*) = *curl* **v** (*x*,*y*,*z*) of the steady subsonic solution is displayed in Figure 9. The *y*-component of **j** points perpendicular into the paper plane. At various downstream positions *x*, the *y*-component of the vorticity in the upper half ($z > 0$) of the flow field behind the respective trailing edge (TE) is integrated from $z/c = 0$ to $z/c = 1$. The result is given in Figure 10. The *x*-coordinate in this figure is counted relative to the respective TE. Except the negative sign, the result in the lower half (not shown here) is equal to the one in the upper half with a very error. Both contributions are supposed to cancel each other like in the limiting case of infinite Reynolds number in 2D "inviscid" theory, where there is no wake at all. The rapid decay of the steady vorticity is surprising, because the unsteady vorticity is conserved much better.

4 UNSTEADY SUBSONIC AND TRANSONIC SOLUTIONS

Figures 11, 12 and 13 show the time history for the lift coefficient c_L, the moment coefficient c_M and the drag coefficient c_D using the parameters in chapter 2. The first two figures display the results for the synchronous harmonic motion of both profiles in subsonic and in transonic flow. The unsteady heaving motion starts with an upstroke at the profiles' mean position $z = 0$. The lift history of the leading profile begins with the maximum negative value just passed at -8 deg. Except a delay in the phase position of about 25 deg for the transonic case, the two lift curves are very similar. The moment coefficients also behave like that. The trailing profile experiences a strong influence for both the subsonic and the transonic case.

The results in Figure 13 are a first approach to a single gust field. The unsteady motion is turned off and both profiles are at rest. The shed wake of the leading profile travels downstream and hits the trailing profile. The behaviour of the corresponding vorticity field is shown in Figure 14. The vorticity is accompanied by a strong vertical flow curling around the *y*-component of **j**, i.e. the gust. The maximum moment each time occurs right after the lift has changed its sign.

The Fourier analysis of the load history in Table 1 shows the load spectrum with significant contributions to lift and moment over a wide range of frequencies:

Harmonic motion				Gust field			
k	Freq	p_cL[%]	cL_abs	k	Freq	p_cL[%]	cL_abs
1	50.02	95.8022	0.229561	1	50.02	78.1246	0.149291
2	100.04	0.0334	0.004286	2	100.04	14.2861	0.063841
3	150.06	3.0980	0.041281	3	150.06	5.0945	0.038123
4	200.08	0.0031	0.001312	4	200.08	1.0918	0.017648
5	250.10	0.3842	0.014538	5	250.10	0.2513	0.008467
6	300.12	0.0081	0.002109	6	300.12	0.3571	0.010093

Table 1: Fourier analysis of c_L of the trailing profile for Ma 0.75. Frequency *Freq*, percentage of contribution *p_cL* and magnitude *cL_abs*.

Finally, first results have been obtained for the 3D gust generator, which basically is the 3D counterpart of the present investigation. The wind tunnel wall is simulated by a viscous wall. The formation of the 3D wake is shown in Figure 17.

5 ACCURACY OF THE UNSTEADY SOLUTION

The propagation of sound waves is represented by unsteady divergence, the propagation and diffusion of momentum, transferred into the fluid from the moving surfaces, by vorticity. The speed of sound waves travelling upstream is estimated from the velocity of sound and the position of a disturbance in two subsequent frames displaying the divergence. Figure 16 is

marked with the displacement of the encircled disturbance during the time interval $T/4$ with $1/T = f$. The distance is roughly 0.44 c, the time interval 5 ms, which results in 88 m/s. From $Ma = 0.75$ and the speed of sound, a slightly different value of 83 m/s is expected, which is a good agreement.

The amplitude of vorticity $j_y(x,z,t)$ and its integral for one cycle of motion, the vanishing circulation $\Gamma = 0$, are calculated at various downstream positions *x-pos* in Table 2. The error *Err*, the ratio of Γ (*Gamma*) to the amplitude *Ampl* of the oscillating vorticity is less than 1 %. Table 2 shows that the amplitude is well preserved.

Wake of the leading profile				Wake of the trailing profile			
x-pos	Gamma	Ampl	Err %	x-pos	Gamma	Ampl	Err %
1.2000	-1.25	62.7	-1.99	6.2000	0.189	85.7	0.22
1.4000	-0.750	57.5	-1.31	6.4000	-0.248	83.2	-0.30
1.6000	-0.310	57.1	-0.54	6.6000	-0.179	83.8	-0.21
1.8000	-0.429	56.1	-0.76	6.8000	-0.261	83.9	-0.31
2.0000	-0.420	55.4	-0.76	7.0000	-0.444	83.4	-0.53
3.0000	-0.431	55.3	-0.78	8.0000	-0.090	82.2	-0.11
4.0000	-0.197	58.0	-0.34	9.0000	-0.096	86.4	-0.11

Table 2: Circulation Γ and vorticity (Ampl) for $Ma = 0.75$ behind both profiles.

6 CONCLUSIONS

The interaction between a gust induced by a profile oscillating upstream and a downstream located profile can well be simulated using the simplification of a synchronous heaving motion. This first approach avoids additional numerical implications caused by the chimera grid generation technique, which needs to be applied for profiles being in motion relative to each other. The constraint will be released in the future work. The accuracy of the computation is investigated using inherent physical properties. The result of the circulation being preserved within an error in the order of one percent indicates a proper setting of the numerical parameters for the numerical computation of the flow field.

7 REFERENCES

[1] Katzmayr, R. (1922). *Über das Verhalten der Flügelflächen bei periodischen Änderungen der Geschwindigkeitsrichtung*, ZFM Heft 6, 13. Jg., 80-82.

[2] Freymann, R. (1985). *Die Böensimulationsanlage des 3m x 3m – Niedergeschwindigkeitskanals der DFVLR in Göttingen*, DFVLR-FB 85-04.

[3] Krag, B., Wegner, W. (1985). *Generation of Two-Dimensional Gust Fields in Subsonic Windtunnels*, in AGARD Conference Proc. 386, AGARD-CP-386, Joint Symposium of the Fluid Dynamics and Flight Mechanics Panels, Göttingen (FRG).

[4] De Bruin, A.C., Schrauf, G. (2007). *Wake Vortex Results From The AWIATOR Project*, CEAS Congress, Berlin, CEAS-2007-008.

[5] Suggested reference for more information: http://tau.dlr.de

[6] Send, W., (2008). *Zum Böenproblem: Ein Ansatz über Interferenz*, DGLR Deutscher Luft- und Raumfahrt Kongress 2008, Darmstadt, DLRK2008-81316.

[7] Send, W. (1995). *Zur Lösung des räumlichen Interferenzproblems in der Instationären Aerodynamik*, DLR-FB 95-42.

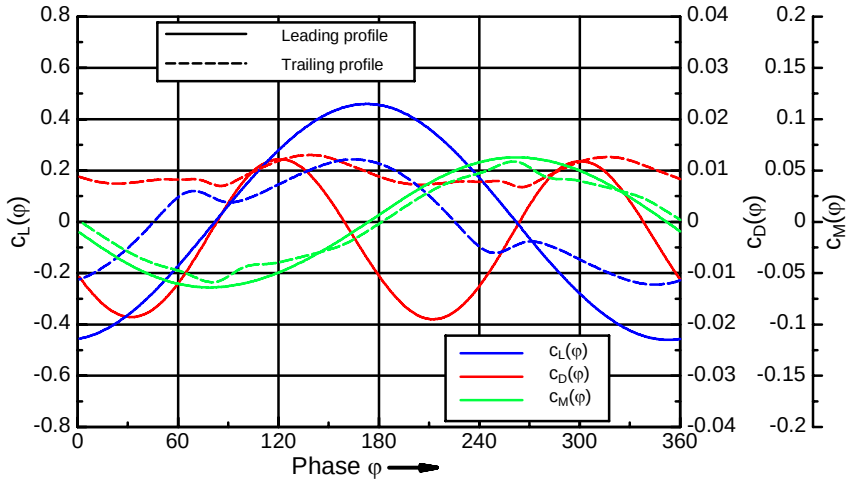

Figure 11: Ma = 0.5, periodic motion in subsonic flow.

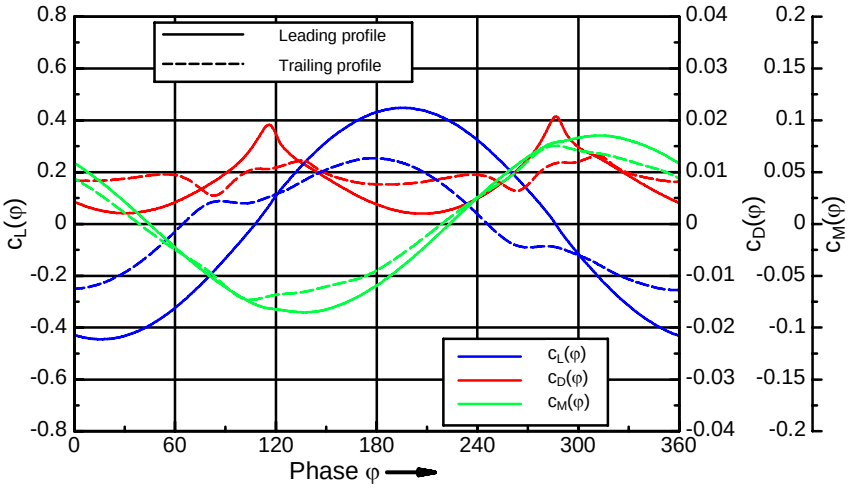

Figure 12: Ma= 0.75, periodic motion in transonic flow.

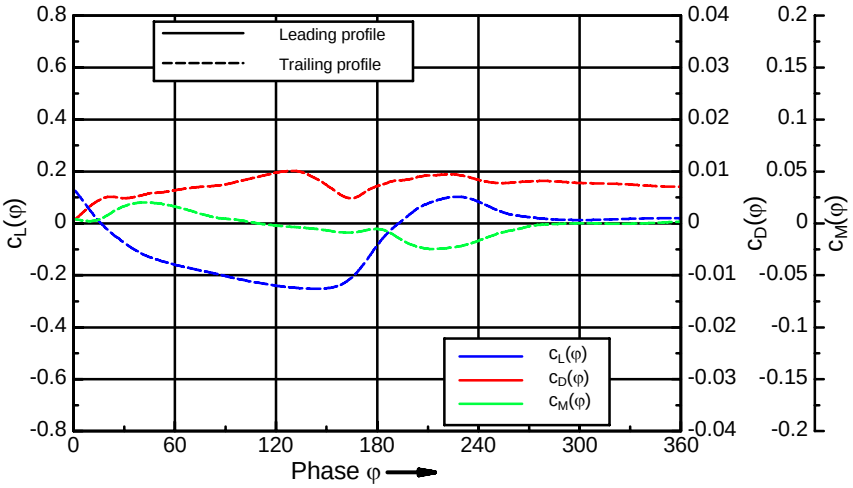

Figure 13: Ma= 0.75, gust field.

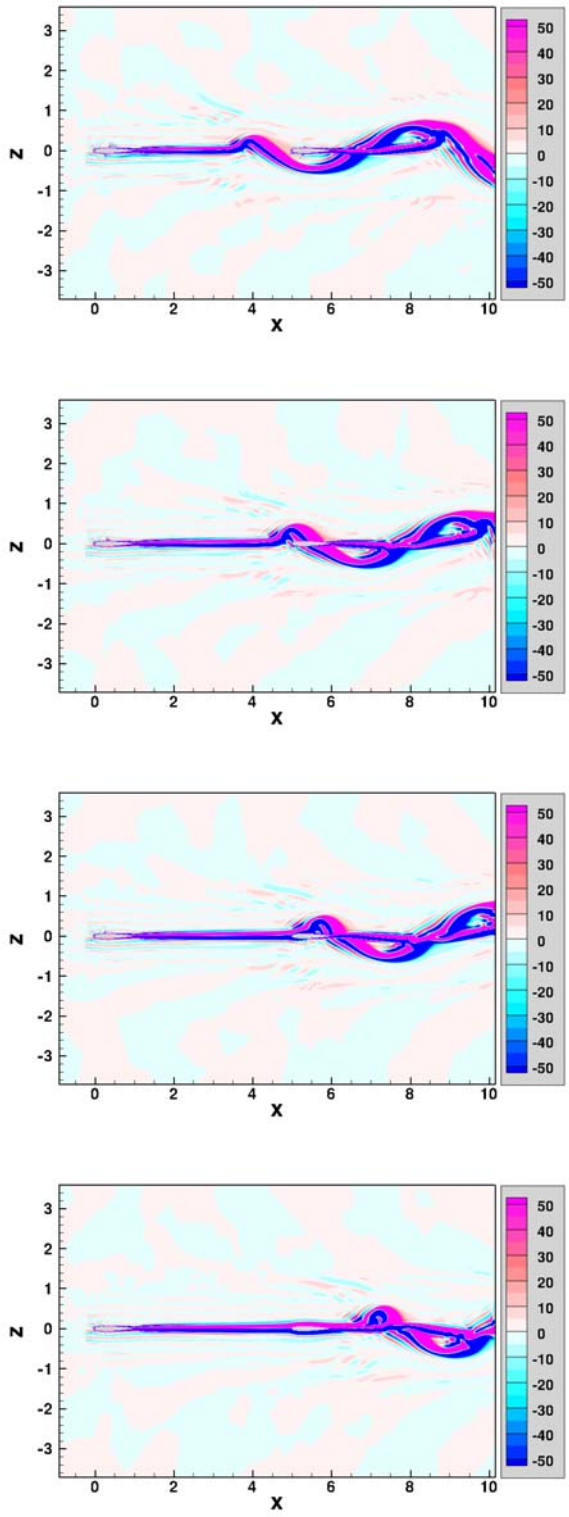

Figure 14: Contours of the vorticity field j_y, ranging from -50 to +50 1/s. Vorticity generated by the leading profile.

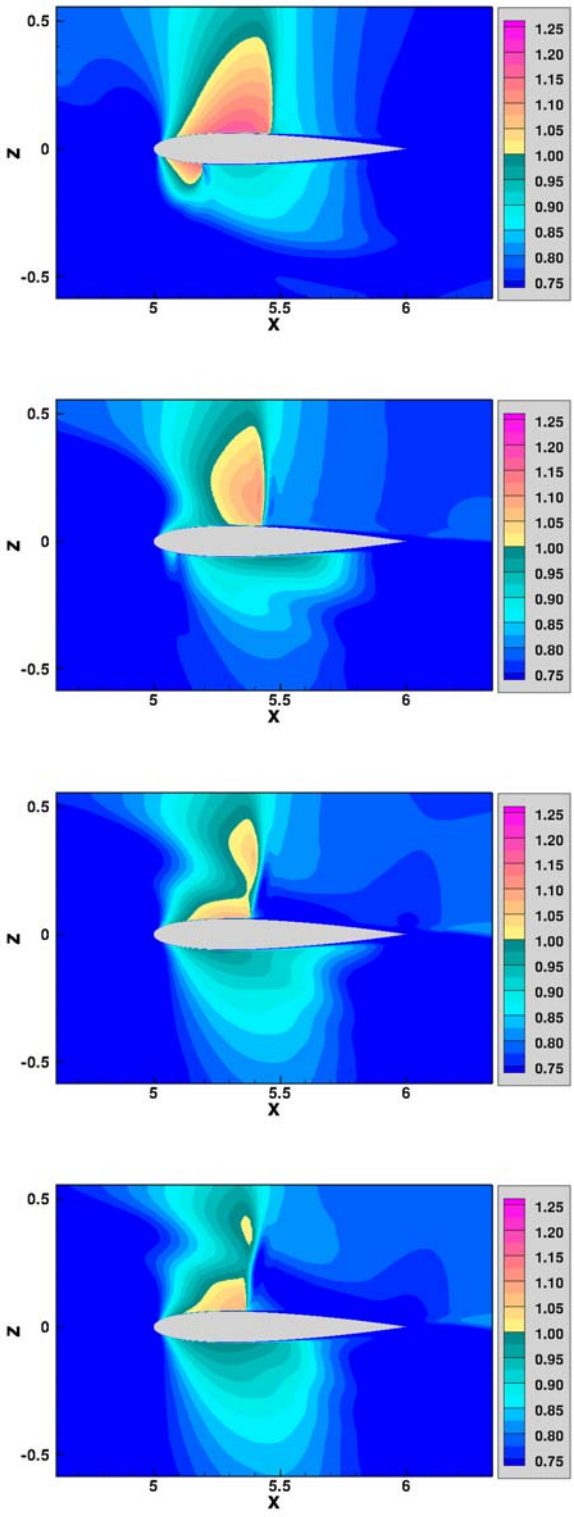

Figure 15: Contours of the Mach number *Ma*, ranging from 0.75 to 1.25. Sequence of frames not related to Fig. 14.

Parameters for both figures: Profile sections NACA0012 without angle of incidence, chord length c = 1 m, space between the profiles 4c, Ma = 0.75, Re = 10^7, amplitude of heaving motion 0.1c, red. frequency ω^* = $2\pi/5$ = 1.257, i.e. a wavelength 5c for the unsteady wake.

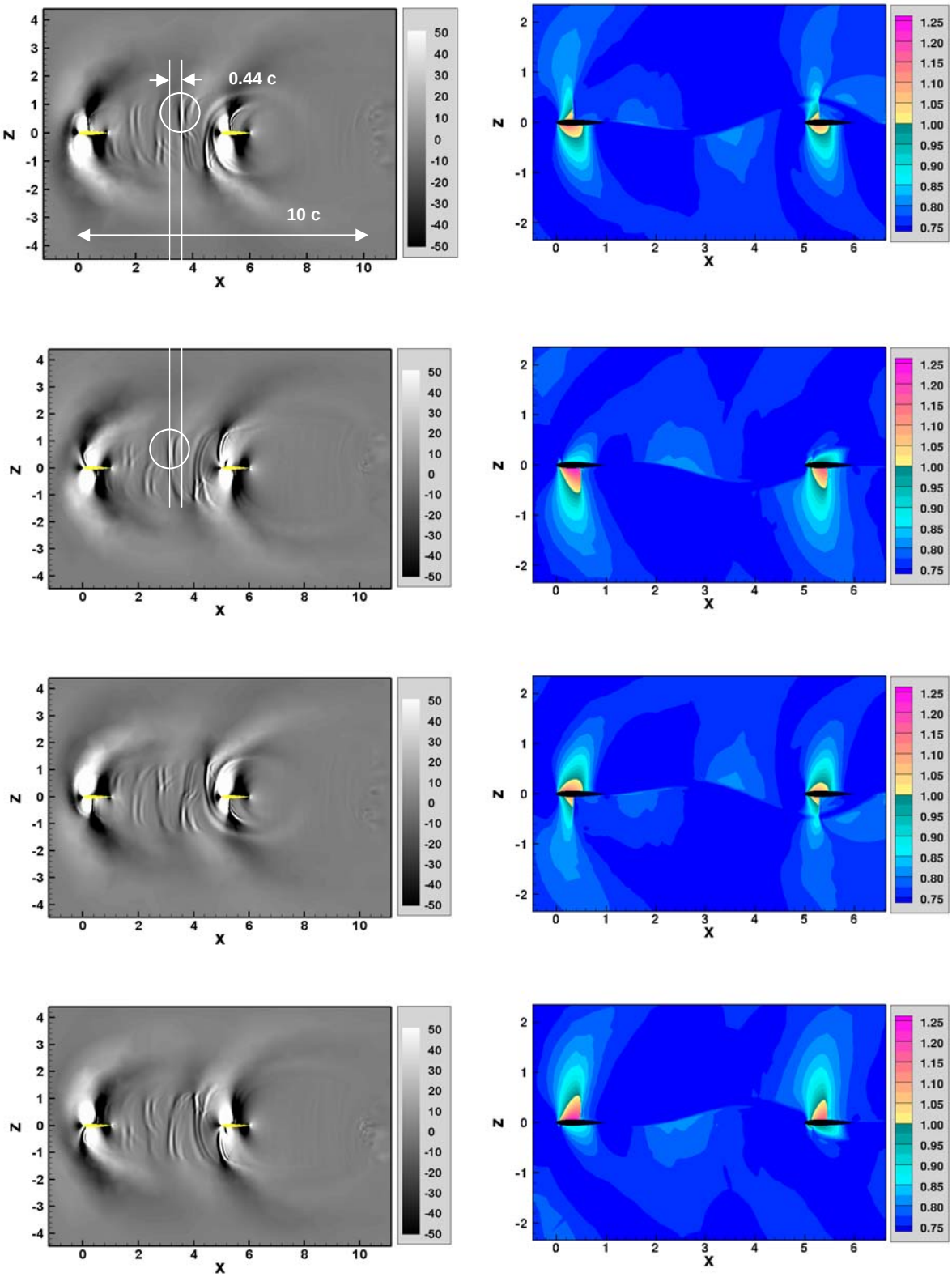

Figure 16: Contours of the functions *div***v** (left) and *Ma* (right) for phase = 0, 90, 180, 270 deg.

Parameters for both figures: Profile sections NACA0012 without angle of incidence, chord length c = 1 m, space between the profiles 4c, Ma = 0.75, Re = 10^7, amplitude of heaving motion 0.1c, red. frequency ω^* = $2\pi/5$ = 1.257, i.e. a wavelength 5c for the unsteady wake.

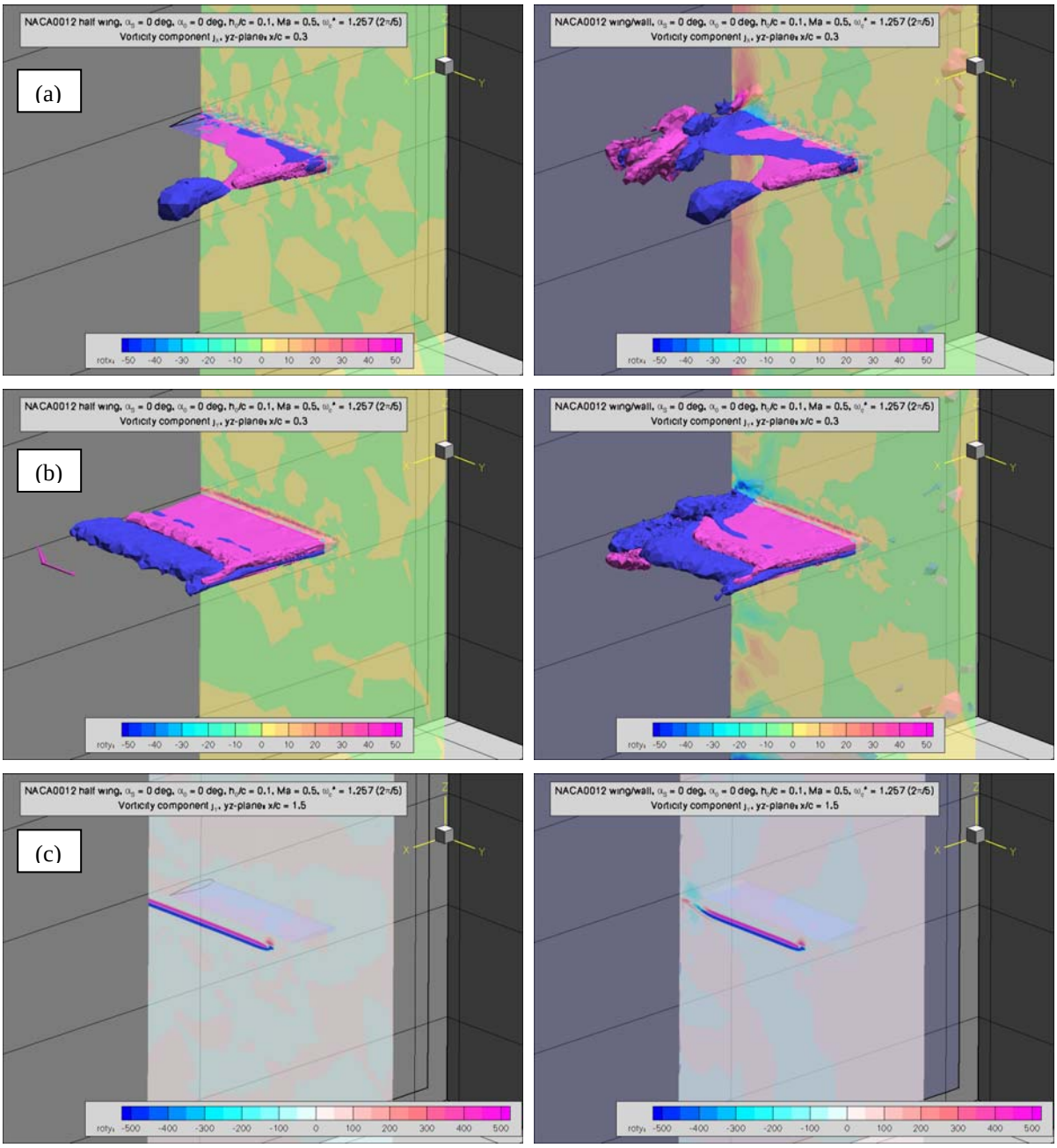

Computation applying symmetry condition Computation applying wing/wall interaction

Figure 17: The vorticity field of the 3D gust generator. View upstream from a downstream position onto the symmetry plane (left column) and the wind tunnel wall (right column) respectively. In row (a) and (b), a cut-plane is located at x/c = 0.3. Downstream of that plane the full view on the iso-surfaces of the x-component in row (a) and on the y-component in row (b). In row (c), the comparison shows a drastic phase shift of the j_Y component close to the wall (right column).

The following two lines show the conservation of circulation for the computation shown. Over one period of motion, the result can separately be computed for both the x and the y-component of vorticity:

Comp	x-Position	Total circ.	Amplitude	Phase	Phase	Phase+90	Rel.err %	Harmonic
j_x	2.0000	-2.07	38.4	163.64	163.64	-106.36	-5.40	0.993095
j_y	2.0000	7.05	76.8	-23.36	336.64	66.64	9.17	0.987442

The fairly high error is caused by a grid which is limited in extend and still is too coarse for a more precise calculation. The wake ceases to exist after about 2 chord lengths where the fine resolution of the wake grid ends.